Microstructural, elemental, mechanical and structural attributes of AA1100/17-4 PH stainless steel composites fabricated via friction stir processing

Tawanda Marazani[a*], Esther. T. Akinlabi[b], Daniel. M. Madyira[a], Jyotsna. D. Majumdar[c] and Surjya. K. Pal[c]

[a]Department of Mechanical Engineering Science, University of Johannesburg, Auckland Park Kingsway Campus, Johannesburg, 2006, South Africa
[b]Pan African University for Life and Earth Sciences Institute, Ibadan, Nigeria
[c]Indian Institute of Technology, Kharagpur, India

A R T I C L E I N F O	A B S T R A C T
	A 100% overlap double pass friction stir process technique was developed for the fabrication of AA1100/17-4 PH stainless steel composites, using an H13 tool steel cylindrical threaded pin with shoulder diameter of 21 mm, pin diameter of 7 mm and pin height of 5 mm. Grooves of 2 mm width and 3.5 mm depth were machined on the 6 mm thick AA1100 plate, where the 17-4 PH stainless steel powder was packed and compacted using a pinless tool. Friction stir processing was conducted at rotational speeds of 2100, 2450 and 2800 rpm, while the travel speed of 20 mm/min, tilt angle of 2.5° and plunge depth of 0.2 mm, were kept constant. Investigations were carried out on the microstructure, elemental composition, and tensile testing and microhardness as well as structural analysis using X-ray diffraction. Defect-free micrographs with good mechanical and metallurgical connections were obtained from all the employed process parameters. However, agglomeration of reinforcements became noticeable at 2450 and 2800 rpm. Uniform distribution of reinforcements were observed at 2100 rpm. Elemental analysis confirmed matrix and reinforcements blending and mixing. Superior SZ hardness of as high as 4 times that of the base metal were achieved, while ultimate tensile strength properties with joint efficiencies as high as 97.29% were attained at 2450 rpm. However, the percentage elongation of the fabricated samples dropped by around 10% due to the reinforcements-induced hardness. Nonetheless, the fabrications retained superior mechanical properties. All the X-ray diffractograms had 5 intense peaks with different phases and crystal planes. However, an Al syn (111) crystal plane was common to all diffractograms at around 39° 2θ range. The obtained crystallite sizes of as small as 4 nm revealed the attainment of ultrafine grains, while the observed high dislocation densities and micro strains gave an indication that the fabricated AA1100/17-4 PH stainless steel composite is of high strength.

1. Introduction

Over the years, there has been growing interest across several metal industries towards the use of lightweight metals, mainly due to their low density, high strength-to-weight ratio and the associated cost-effective benefits. Among these, aluminium (Al) and its alloys, offer the much needed benefits, hence their present standing as workhorse metals for multiple industrial applications. Aluminium alloys are well known for their low density of around 2.7 g/cm^3, abundance, high strength-to-weight ratio, ability to resist oxidation and to self-heal when scratched, good corrosion resistance, good appearance, high

workability, easy processing, as well as high thermal and electrical conductivities (Kumar, et al., 2020; Pai, et al., 2020; Bourkhani, et al., 2019). As a result, aluminium and its alloys have earned a household name in the aerospace, automobile, marine, defence and infrastructural building industries (Rao, et al., 2020; Mehtedi, et al., 2017; Chelladurai, et al., 2020), replacing many steel industrial applications (Adamowski & Szkodo, 2007). However, of the aluminium alloy grades, pure aluminium grades have not been so actively used in areas where superior surface attributes are key load bearing requirements, despite their high workability. Pure aluminium exhibits inferior tribological attributes as a result of its low hardness, low strength and high resistance to friction, which have been major limitations for its end applications (Rahmati, et al., 2020; Sampath, et al., 2015).

To mitigate the limitations, increasing industrial demands for materials with unique properties have prompted the development of industrial-needs-based surface composites (Dutta, et al., 2019). There are three main categories of composites, namely, the ceramic matrix composites (CMCs), metal matrix composites (MMCs), and polymer matrix composites (PMCs), while a base matrix with two or more reinforcements forms a hybrid composite (Singh & Belokar, 2020). (Mhaske & Shirsat, 2020), defined a composite as a material formed by two or more macro insoluble components, with different shape and elemental composition, wherein, the discrete component is termed the reinforcement, while the base material or the continuous phase is called the matrix. To date, various surface treatment techniques have been developed (Liu, et al., 2020), and these include; alloying, coating (Rahmati, et al., 2020; Chelladurai, et al., 2020), stir casting (Narayana, et al., 2020) and squeeze casting, infiltration, and powder metallurgy (Mhaske & Shirsat, 2020), laser melting or cladding and Additive Manufacturing (Srivastava, et al., 2021; Bourkhani, et al., 2020), accumulative roll bonding, and the vortex method (Bourkhani, et al., 2019), powder blending and consolidation, physical vapour deposition, diffusion bonding, spray deposition and in-situ processing (Chelladurai, et al., 2020). Surface composites are developed to meet combinations of some of the listed attributes, namely: high toughness, high strength, superior wear resistance, excellent corrosion resistance, density, creep resistance, dimensional stability, stiffness, high electrical conductivity, high thermal conductivity, high hardness and improved microstructure (Yunusov, et al., 2020; Mhaske & Shirsat, 2020; Mehta & Vadher, 2020; Alishavandi, et al., 2020). These attributes are usually unattainable by a single material (Zamani, et al., 2020; Akinwamide, et al., 2021; Gunasekaran, et al., 2020; Shuvho, et al., 2020).

Amongst the existing methods for developing aluminium based composites, is a green technology known as friction stir processing (FSP), a technique with so many benefits, which include; no requirement for surface cleaning, good dimensional stability, improved repeatability, low parts distortion, refined and homogenized grains, no chemical effects, solid-state process, highly energy efficient, produces no fumes, produces less noise and no requirements for cleaning worked surfaces (Miranda, et al., 2013). Friction stir processing is a solid-state materials processing technique that was developed at The Welding Institute (TWI) in 1999, through the works of Wayne Thomas, from improvements made on friction stir welding (FSW), a technology that he had invented and patented earlier, in 1991 (Ikumapayi, et al., 2020; Kiran & Pravala, 2017; García-Vázquez, et al., 2017; Padhy, et al., 2018). Reinforced FSP incorporates second phase particles to locally modify the processed zones through severe plastic deformation and material mixing, which results in grain refinement, improved microstructure and superior mechanical and metallurgical integrities. The technique is conducted based on the FSW principles, the only difference being that, FSP does not have a joint interface (Kumar M, et al., 2017; Kumar, et al., 2017; Ju, et al., 2017).

Friction stir processing is governed by numerous carefully considered process parameters, which include, base material, tool design, tool tilt angle, tool rotational speed, tool travel speed, plunge depth, reinforcements type and delivery method, and tool forces, among other key parameters (Kumar M, et al., 2017; Marazani, et al., 2020). Presently, FSP has vast applications in the defence sector, aerospace, marine, chemical, transportation and automobile industries where surface composites are highly

exploited for meeting various combinations of physical, mechanical and metallurgical requirements (Dutta, et al., 2019; John, et al., 2016). Innumerable Al based in-situ, surfaces, in-volume or bulk level micro, nano, and hybrid composites have been developed via friction stir processing (Rahmati, et al., 2020; Ikumapayi, et al., 2020; Dutta, et al., 2019). Various Al grades and particulates have been used as matrix and reinforcements respectively. The commonly used reinforcements in aluminium alloys include, SiC, Aluminium Nitrate, TiB_2, Rice husk ash, fly ash, Graphite, ceramic, piezoelectric ceramic powder (PZT, $BaTiO_3$) (Dutta, et al., 2019; Mhaske & Shirsat, 2020; Narayana, et al., 2020; Padhy, et al., 2018), fullerene soot (Yunusov, et al., 2020), Al_2O_3, B_4C (Akinwamide, et al., 2021), WC, TiO_2, MgO, Gr, carbon nanotubes (CNTs) and steel fibres (Chelladurai, et al., 2020), coconut shell ash (CSA) (Ikumapayi, et al., 2020), Fe_3O4 powder (Mehta & Vadher, 2020), Zirconium dioxide (ZrO_2) (Gunasekaran, et al., 2020), Mg, Si (Kumar, et al., 2017), and coal fly ash (CFA), wood fly ash (WFA), cow bone ash (CBA), palm kernel shell ash (PKSA) (Ikumapayi & Akinlabi, 2019), due to the wide range of properties of interest which include, superior hardness, improved stiffness, and wear resistance, among others. However, for this work, interest is placed on pure aluminium based composites which have been hardly studied and published, where few emerging works from recent publications were noticed, hence the focus of the present work. It is noteworthy that the used reinforcements depend on the required surface treatment and the expected properties to be attained according to the in-service conditions and environment that the fabricated composites will be expected to safely withstand. Use of stainless steel powder as a reinforcement has also been noted in emerging research works. (Ikumapayi & Akinlabi, 2019), reinforced AA7075-T651 aluminium with 17-4 PH stainless steel and the results obtained were reported to exhibit improved mechanical and metallurgical attributes. (Marazani, et al., 2020), also reinforced AA1100 aluminium with 17-4 PH stainless steel powder, which is an extension of the present work. 17-4 PH stainless steel is a martensitic precipitation-hardening steel grade with high strength, excellent corrosion resistance, good weldability, formability, mechanical, thermal and magnetic attributes, which made it the most prominently used among all the precipitation-hardening stainless steels (Bayode, et al., 2017). Pure aluminium has low mechanical properties, but its strength can be enhanced through strain hardening since it has high workability, which opens room for its easier localized manipulation through friction stir processing. It softens when thermo-mechanically worked, like in the case of friction stir processing, hence the need for reinforcements. Few emerging studies on FSP of pure aluminium are, therefore, reviewed in Table 1.

In structural studies conducted on AA7075-T651/17-4 PH stainless steel composites developed via friction stir processing, (Ikumapayi, et al., 2020) used the Scherrer equation, in Eq. (1.1), to confirm the acquired crystallite size, Williamson-Hall equation, in Eq. (1.2), to confirm the acquired micro strain, and calculated the dislocation density using Eq. (1.3). Where: C = the crystallite size, k is the shape factor, and = 0.94 for pure aluminium, λ = wavelength and = 1.5046 (Å), β = the FWHM (°), θ is the Bragg's angle (°), ε = micro strain and **δ** = dislocation density.

$$C = \frac{k\lambda}{\beta Cos\theta} \tag{1.1}$$

$$\varepsilon = \frac{\beta Cos\theta}{4} \tag{1.2}$$

$$\delta = \frac{1}{C^2} \tag{1.3}$$

On one hand, 17-4 PH stainless steel exhibits superior mechanical attributes that are ideal for many applications, with great potential to soundly reinforce friction stir processed pure aluminium, yet still very much unexplored. On the other hand, pure aluminium is highly workable and stands to be one of the cheapest aluminium alloys. Furthermore, FSP of pure aluminium based composites, is not so broadly studied, with very few emerging published research works. Out of the few reported pure aluminium based

composites fabricated via FSP, AA1100/17-4 PH stainless steel composites have not been studied and published. The novelty of this work is therefore to exploit these research gaps, the flexibility and potential of FSP, the workability of AA1100 as the continuous phase and the excellent mechanical properties of 17-4 PH stainless steel powder as the reinforcement, and develop composites using the two.

Table 1. Review of emerging pure aluminium based composites produced through friction stir processing

Authors	Matrix	Reinforcement	Materials and Process Parameters	Findings
(Alishavandi, et al., 2020)	AA1050	30 nm Mischmetal oxide (MMO)	H-13 threaded (0.5 mm depth and 30° angle, and nutting angle of 2.5°) tool, shoulder diameter 18 mm, pin diameter 5 mm, pin height 3.5 mm, 3° tilt angle, 4 mm thick plate, groove depth, width, and length of 3, 1, and 210 mm respectively and 6-passes at 1600 rpm, 100 mm/min.	Homogenously distributed reinforcement particles, 120% increase in UTS and 130% in hardness, 17% drop in Coefficient of friction (COF) and 40% drop in wear rate compared with the base metal (BM), Adhesive wear mode for the BM and abrasive wear mode for the AA1050/MMO composite, and improved corrosion resistance.
(Reddy, et al., 2020)	99% CP Al	--	5 mm plate, H13 taper tool, shoulder diameter of 15 mm and 4 mm pin length, 600 rpm and 60 mm/min, 10 kN axial load.	Fine and fully recrystallized grains with an average SZ grain size of 6.79μm, excessive FSP generated heat which softened the stir zone by dropping the dislocation density and caused hardness to decrease by 27%. Increased damping capacity at temperatures more than 130°C, due to increased grain boundary area from the microstructure refinement.
(Bourkhani, et al., 2020)	AA1050	100 nm Al_2O_3	Plate of 10×100×50 mm, thickness by length by width. 1×3 mm width and depth groove. H13 tool steel, shoulder diameter 20 mm, pin height 5 mm, pin diameters of 4, 6 and 8 mm, 3° tool tilt angle, 0.3 mm plunge depth. Single and double pass processing at 1180 rpm and 80 mm/min.	Improved ductility due to grain refinement. Uniform distribution of nanoparticles in the formed composite. Strength and flow stress higher than that of the BM. Single pass FSP cannot effectively distribute reinforcements and is susceptible to reinforcements agglomeration, which reduces ductility. Highest ductility was achieved using the 6 mm pin.
(Bourkhani, et al., 2019)	AA1050	Al_2O_3	100×150×10 mm plates. annealed at 510 °C for 1 hr, cooled in the furnace. Al_2O_3 nano powder dried for 1 hr at 40 °C. Plate groove of 1 mm in width and 3 mm in depth. Groove filled up with nano powder to 2 mm. H13 tool steel heat treated tool, 20 mm shoulder diameter, pin diameter, 6 mm, 5 mm height, 1180 rpm rotational speed, travel speed 80 mm/min, 3° tilt angle and 0.3 mm plunge depth, double pass FSP.	Excessive stirring caused the finest grains to be formed in the second region from the top surface. Single pass FSP could not uniformly distribute particles in the bottom surfaces, leading to particle depleted regions (PDRs) and coarse agglomerated particles being formed. Agglomeration transformed tensile fracture from ductile to brittle. Second FSP pass yielded uniform particle distribution, grain refinement, improved tensile and tribological properties, and reduced coefficient of friction (COF).
(Alishavandia, et al., 2020)	H14 AA1050	50 nm MMO	195 × 65 × 4 mm plate, groove width, depth, and length Of 2, 3.5, and 195 mm, respectively. Reinforcements compacted with a 10 m diameter pinless tool at 900 rpm, and 60 mm/min. Heat-treated H13 steel tool, FSP done at 800 -2000 rpm 50-200 mm/min, and tilt angle of 3°.	In-situ solid-state chemical reactions between the Al matrix and the MMO particles. Multi-pass FSP yielded uniform distribution of particles, decreased agglomeration, UFG microstructure, high tensile properties 180% (YS=70 MPa) and 120% (UTS=132 MPa), reduced ductility from 35% to 23% and ductile-brittle fracture mode.
(Wang, et al., 2020)	AA1060	Q235 Steel	6 mm thick plate, 1:1 thickness ratio of aluminium to steel, 25 mm shoulder diameter,7 mm pin diameter, at 1000 rpm counter clockwise rotation and 30 mm/min,	Enhanced mechanical properties at 3 passes, at an overlap (l/d) set at 5/25. FSP repaired aluminium/steel composite plate interface defects, improved composite bonding strength through metallurgical interconnection. Grain refinement yielded improved interface bonding strength.

Strengthening or reinforcing AA1100 with 17-4 PH stainless steel powder is likely to eliminate its softening challenge and, once worked, improve its mechanical and metallurgical attributes with the potential to develop composites that could withstand a number of in-service, physical and environmental requirements, all which cannot be attained by AA1100 aluminium alone. Moreover, the rotational speeds employed in this work are much higher than those used in similar works reported in the consulted literature, while the chosen ranges of travel speeds are much lower and the physical dimensions of the tool are much bigger than the reported values. These altogether give a hallmark of originality to the present work, whose results will also serve as an additional contribution to the existing knowledge.

2. Materials and Methods

2.1 Materials

In this study, wrought rolled AA1100 sheets of dimensions 500×600×6 mm were used as the parent metal. The sheets were supplied by Bharat Aerospace Metals without the certificate of composition, and energy dispersive X-ray (EDX) was used for elemental analysis in order to ascertain the supplied AA grade before its use in the present work. The EDX results obtained are shown in Fig. 2.1. Ideally, AA1100 comprises between 99.0 - 99.95% Aluminium (Al), with the remainder being distributed among alloying elements and residuals. These principal impurities were reported by (Vijayasarathi & Selvam, 2014) to be, 0.05 - 0.2% Copper (Cu), ≤ (0.95% Iron (Fe), 0.05% Manganese (Mn), 0.95 Silicon (Si), 0.1% Zinc (Zn)), while residuals take up 0.15%. Although the alloying elements and residuals were not detected, the results obtained from the conducted tests confirmed that the supplied grade was indeed commercially pure aluminium. Absence of these could be attributed to the fact that they were not added by the supplier during the manufacturing process.
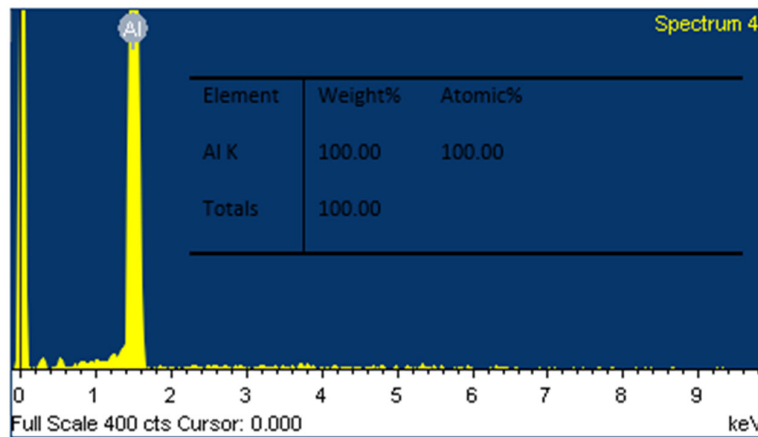

Fig. 2.1. Energy dispersive X-ray of the AA 1100 sheet

The AA1100 sheets were cut to dimensions 250×120×6 mm, using a water based cutter in order to suppress thermal effects of the cutting process. As shown in Fig. 2.2, rectangular grooves with length by width by depth of 220×2×3.5 mm respectively were slotted on the cut AA1100 sheets. The 17-4 PH stainless steel powder of average size that ranged from 45-90μm was packed into the rectangular grooves and in order to inhibit powder ejection from the groove during friction stir processing, a pinless tool was employed to compact the powder within the AA1100 plate groove. The elemental composition of the 17-4 PH SS powder is shown in Table 2. The pinless tool was made of H13 tool steel and had a pin diameter of 21 mm as shown in Fig. 2.3, where all indicated dimensions are in mm.

Table 2. Elemental composition of 17-4 PH SS powder

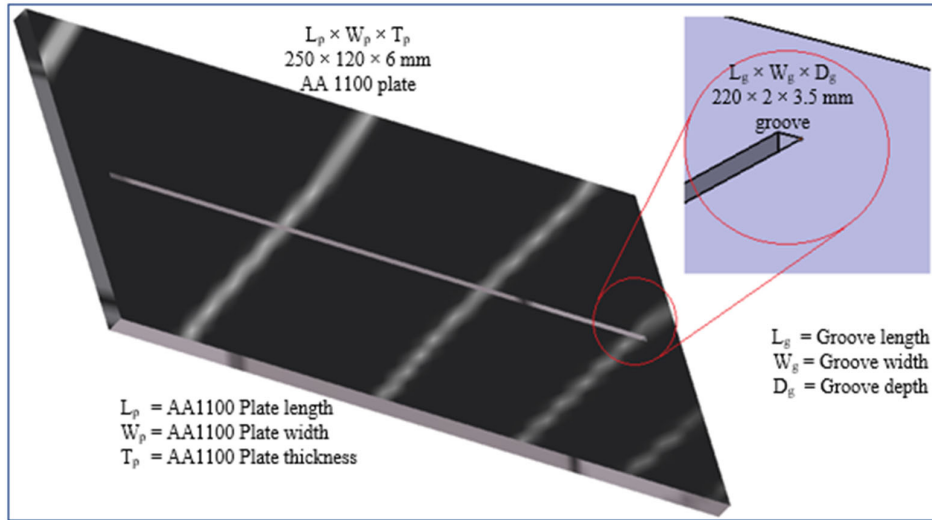| Elements	Fe	Ni	Cr	Cu	C	Mn	P	Si	Nb	S
Wt. % Composition	73.461	3.864	16.564	3.850	0.010	0.953	0.038	0.977	0.264	0.027

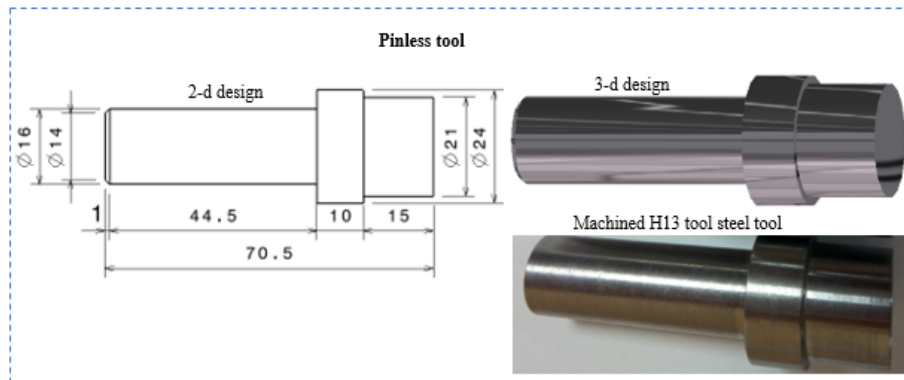**Fig. 2.2.** Schematic representation of the grooved AA1100 plate

Fig. 2.3. Pinless compaction tool

Friction stir processing was carried out using the 3-axis 2T ETA Friction Stir Welding machine, shown in Fig. 2.4. A cylindrical left hand threaded pin tool of 1 mm pitch and other specifications shown in Fig. 2.5, was designed and machined for the friction stir process. It is important to note that all dimensions indicated in the figure are in mm.

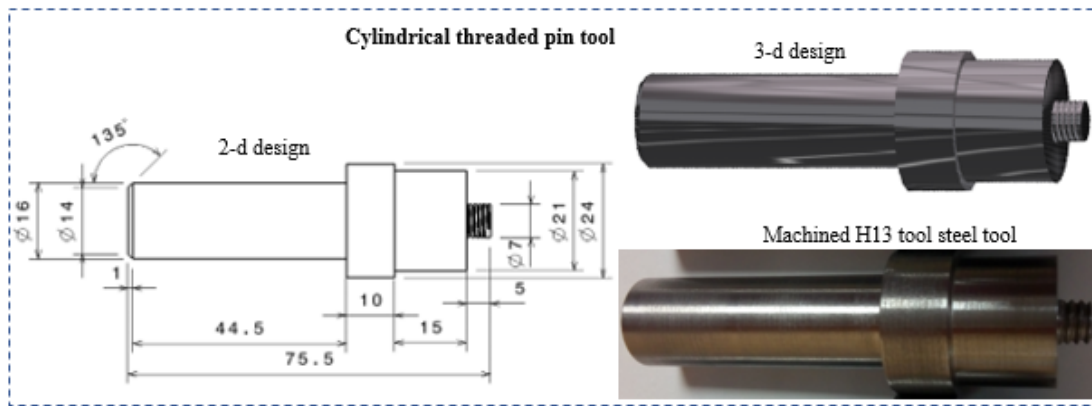**Fig. 2.4.** 2T ETA Friction Stir Welding Machine

Fig. 2.5. Cylindrical threaded pin tool

The grooved AA1100 sheet was firmly clamped onto the machine working table as indicated in Fig. 2.6. 17-4 PH stainless steel powder was packed into the grooves for subsequent compaction with the pinless tool. Single pass friction stir compaction was conducted at a rotational speed of 900 rpm, 1° tool tilt angle, 40 mm/min travel speed and 0.1 mm plunge depth. In addition, 100% double pass friction stir processing was carried out using parameters summarized in Table 3.
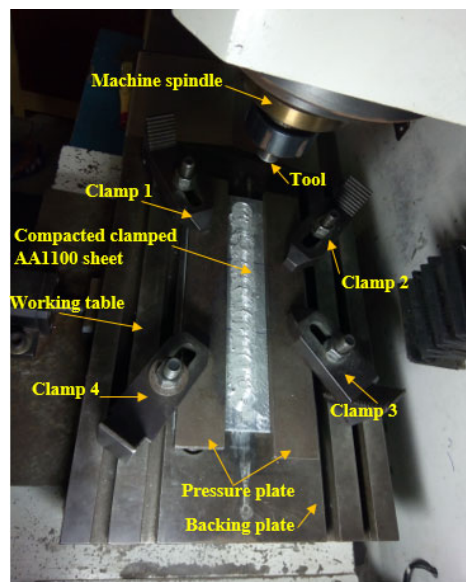

Fig. 2.6. Job setup showing the compacted AA1100 sheet

Table 3. Friction stir process parameters

Rotational speed (rpm)	Travel speed (mm/min)	Tilt angle (degrees)	Plunge depth (mm)
2100	20	2.5	0.2
2450	20	2.5	0.2
2800	20	2.5	0.2

2.2 Microstructural Attributes – Optical Microscopy and Scanning Electron Microscopy

Optical microscopy (OM) – These studies were conducted on the Olympus DP25 microscope at magnifications that ranged from 5X to 100X, while parfocal objectives of (0.5X, 1.0X, 1.6X and 2X) were conducted using the Olympus SZX16 microscope, fitted with a 6V tungsten halogen bulb. Both

microscopes were interfaced with a personal computer equipped with Olympus Stream Microsoft-integrated image processing software.

Scanning Electron Microscopy (SEM) – Higher resolution topographical analyses of the friction stir processed samples were conducted using the TESCAN VEGA3 Scanning Electron Microscope, a modern, wholly PC-interfaced machine, which utilizes a heated tungsten filament, operates in nanospace and which runs on VegaTC software. SEM-EDS analyses were carried out under high vacuum mode and high accelerating voltage (20 kV) due to the high electrical conductivity of pure aluminium (35 MS/m at room temperature), and also due to the bulkiness of the Al samples. All micrographs were acquired using the backscattered electron (BSE) detector in order to obtain in-depth signal of the analysed samples. Live SEM micrographs were obtained in both wide view and resolution modes using scanning speed 3 continual at a working distance of 15 mm, beam intensity of 14 and were acquired at scanning speed 6 single.

2.3 Elemental Attributes – Energy Dispersive Spectroscopy (EDS)

The TESCAN VEGA3 Scanning Electron Microscope was equipped with an EDS detector. Energy dispersive spectroscopy analysis was conducted using Oxford 1 Aztec software and in closed camera mode. It was used for elemental composition and quantification. The working principle of EDS is such that the sample surface or spectrum gets scanned across by the SEM electron beam. It produces X-ray fluorescence from the atoms along its path and each X-ray photon energy level amounts to the element from which it originated. These put together by EDS microanalysis inbuilt framework, are categorised, named and plotted according to the peaks of the respective energy distributions.

2.4 Mechanical Attributes – Tensile Testing and Microhardness Profiling

Tensile Testing – The 6 mm thick Subsize tensile test specimens were drawn using CATIA P3 V5R14 software. They were designed according to the ASTM B557M – 15 Standard Test Methods for Tension Testing Wrought and Cast Aluminium- and Magnesium-Alloy Products (Metric) (ASTM-International, 2015), and were cut from the fabricated samples as shown in Figure 2.7. The tensile test specimens were subjected to tensile testing using the Zwick/Roell Z250 tensile testing machine, at an extension rate of 5 mm/min.
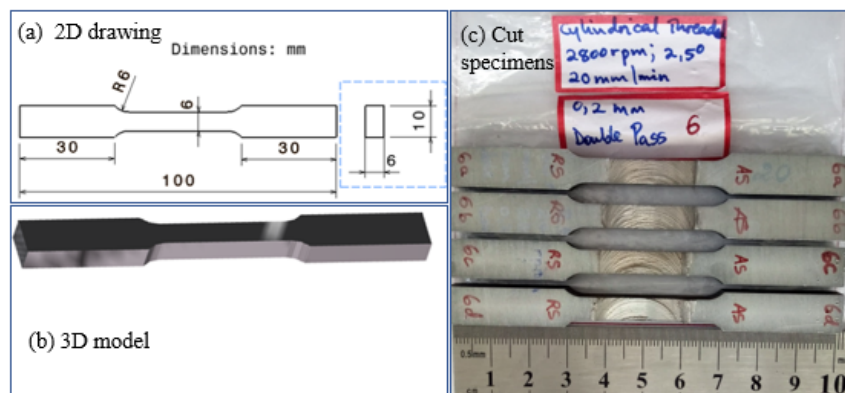

Fig. 2.7. Subsize tensile test specimen

Microhardness Testing – Vickers microhardness (HV 0.2) testing of the mounted, grinded and polished friction stir processed samples was conducted using the Micro Met Scientific cc digital microhardness tester equipped with a diamond indenter. The tests were carried out according to ASTM Designation E92-17 (ASTM-International, 2017) using a 200 g force at 15 seconds dwell time, maintaining indentation intervals of 1 mm for all the measurements that were made. Microhardness measurements were taken across all the friction stir zones, in order to obtain refined hardness trends across the whole sample. This was done following the microhardness design pattern shown in Fig. 2.8.
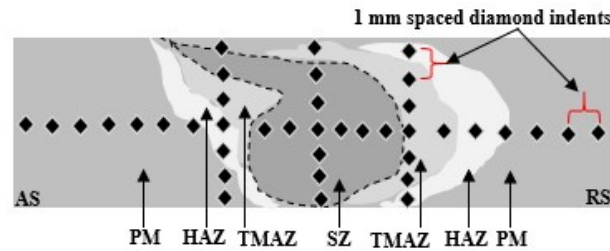
Fig. 2.8. Microhardness test pattern

2.5 Structural Analyses – X-ray Diffraction

X-ray diffraction studies were conducted using the HighScore software run X'PERT X-ray diffraction machine. The measurement conditions used included, a K-beta filter with anode excitation voltage and current settings of 40 kV and 30 mA respectively, scintillation counter detector, continuous scanning mode, scan speed of 1°/min, step width of 0.01°, 2Theta/Theta scan axis, scan range of 5° to 90°, incident slit and receiving slit #1 of 2/3°, and an open receiving slit #2. The obtained X-ray diffraction patterns, crystallite phases present, crystallite size and micro strain studies constituted the structural analyses.

3. Results and discussion

The results obtained from the conducted characterizations and tests are presented in the subsections that follow.

3.1 Optical Microscopy and Scanning Electron Microscopy Examinations

Optical microscopy – The macrographs for the fabricated samples with no visible defects and that clearly revealed all the friction stir processed zones, are shown in Fig. 3.1. It was observed on all macrographs that the heat affected zone (HAZ) was larger on the retreating side (RS) compared to that on the advancing side (AS) and that the thermo-mechanically affected zone (TMAZ) was symmetrical about the stir zone (SZ). All the nugget zones (NZ) or Stir zones had identical rounded convex basins, with the 2450 rpm SZ showing the onion ring as shown in part (b) of the figure. Onion rings, represented by concentric circles in the SZ are formed as a result of the combined effect of tool rotation and translation. SZs are categorised as wide-top basin, and elliptical, which are generated as a result of the effects of the employed process parameters, mainly the tool pin profile, and the thermal energy induced onto the pin and into the plate (Anand & Sridhar, 2019).

In the present work, the rounded convex basins could be attributed to the large pin diameter (7 mm) that was employed. The basin SZ was formed as a result of the extreme deformation and shoulder frictional heating at the upper surface of the processed zone. Well mixed matrix and reinforcement particles were also observed in the NZ. All the macrographs had visible flow arms (FA) on the AS, towards the top of the friction stir processed zone, while hooks can also be observed on both sides of the AS and RS of processed zones. These confirm fabrications with good mechanical and metallurgical connections, which are expected to exhibit superior attributes (Kumar & Praveen, 2017). Rearrangement of particles in the SZ of all samples also shows the capability of FSP to locally modify the processed zones, through severe plastic deformation and material mixing (Marazani, et al., 2020; Ikumapayi, et al., 2020).

Microstructural studies were further conducted on the fabricated samples in order to get more details about the morphology of the samples. Figs.s 3.2 – 3.4 show defect free micrographs of the fabricated samples, which confirmed that the adopted process parameters represented a good process window for the friction stir process. The micrographs were characterized by almost uniform mixing of the matrix and the reinforcement particles, consistent with findings made in literature (Elfar, et al., 2016). Visible traces of plastic flow and material stirring can be seen on all the micrographs. Uniform mixing of the matrix

and the second phase particles indicate successful impregnation of reinforcements, which usually yields superior mechanical properties (Mouli, et al., 2017). The precipitates (white contrast) observed on the micrographs could be the dispersed iron particles. The observed circular particles could be as a result of the high rotational tool stirring action at low travel speed which resulted in high processing pitch and more heat input that caused a rolling effect to the material. The elongated particles could be attributed to the pulling effect of the traversing tool, while the irregular shaped grains could have been formed as a result of the random deformation and mixing of the plasticized material during friction stir processing.
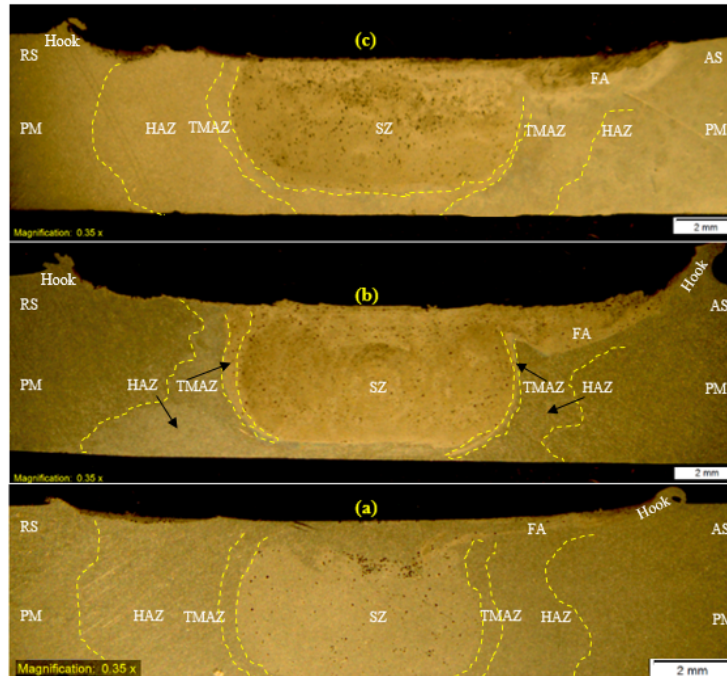

Fig. 3.1. Macrographs of the friction stir processed samples processed at travel speed 20 mm/min, 2.5° tool tilt angle and 0.2 mm plunge depth at rotational speeds: (a) 2100 rpm, (b) 2450 rpm and (c) 2800 rpm
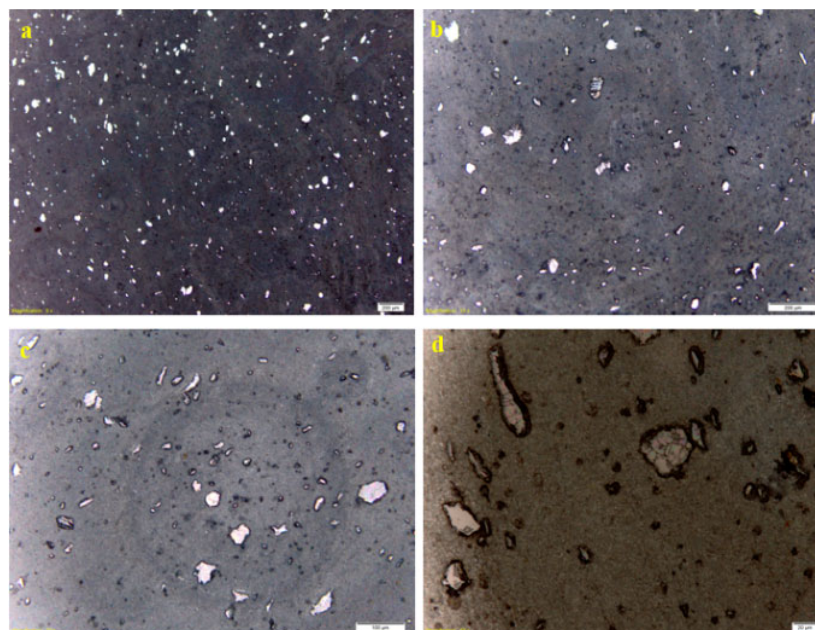

Fig. 3.2. Micrographs for samples processed at 2100 rpm, 20 mm/min, 2.5° and 0.2 mm plunge depth, at magnifications: (a) 5 x, SZ, (b) 10 x, SZ, (c) 20 x, SZ-TMAZ interface and (d) 50 x, SZ-TMAZ interface
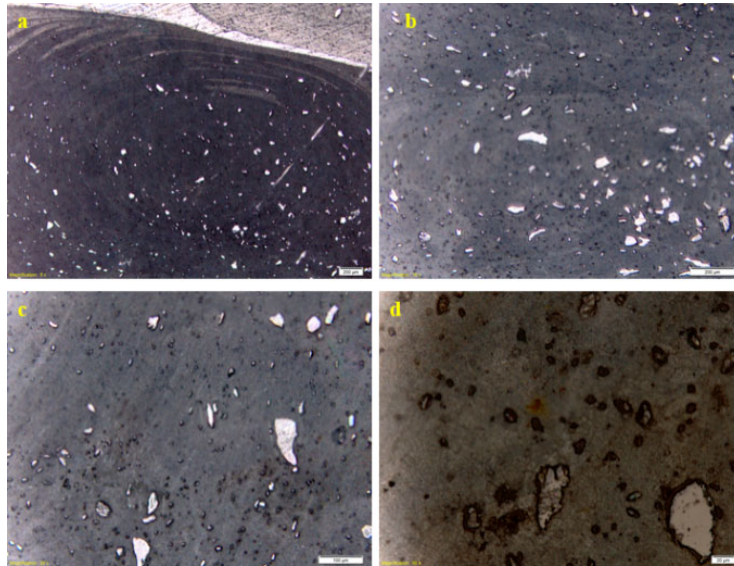
Fig. 3.3. Micrographs for samples processed at 2450 rpm, 20 mm/min, 2.5° and 0.2 mm plunge depth, at magnifications: (a) 5 x, SZ-TMAZ-HAZ-BM bottom interfaces (b) 10 x, SZ (c) 20 x, TMAZ-SZ interface and (d) 50 x, TMAZ-SZ interface
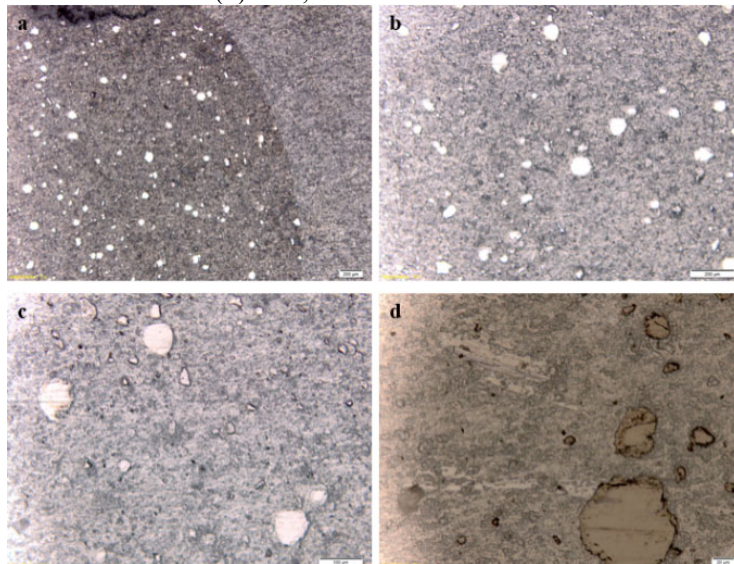

Fig. 3.4. Micrographs for samples processed at 2800 rpm, travel speed 20 mm/min, 2.5° and 0.2 mm plunge depth, at magnifications: (a) 5 x, SZ-TMAZ-HAZ-BM interfaces (b) 10 x, SZ,(c) 20 x, TMAZ-SZ interface and (d) 50 x, HAZ-TMAZ-SZ interfaces

Scanning electron microscopy – 2100 rpm_20 mm/min processed micrographs: Fig. 3.5 and Fig. 3.6 show defect free micrographs, dominated by well mixed matrix and reinforcements, and refined grains in the SZ and the TMAZ. Reinforcements (white contrast) were homogeneously dispersed in the NZ and the TMAZ, which is a known feature of multi-pass friction stir processing (Mahmoud & Tash, 2016). All the micrographs had defect-free smooth mechanical and metallurgical connections between the SZ – TMAZ – HAZ – BM interfaces. Plastic deformation patterns of the plasticized material as a result of the tool stirring effect, were also observed. Grains had a mixture of elongated, round and irregular grains. Their causes were reported in the earlier section on optical microscopy.
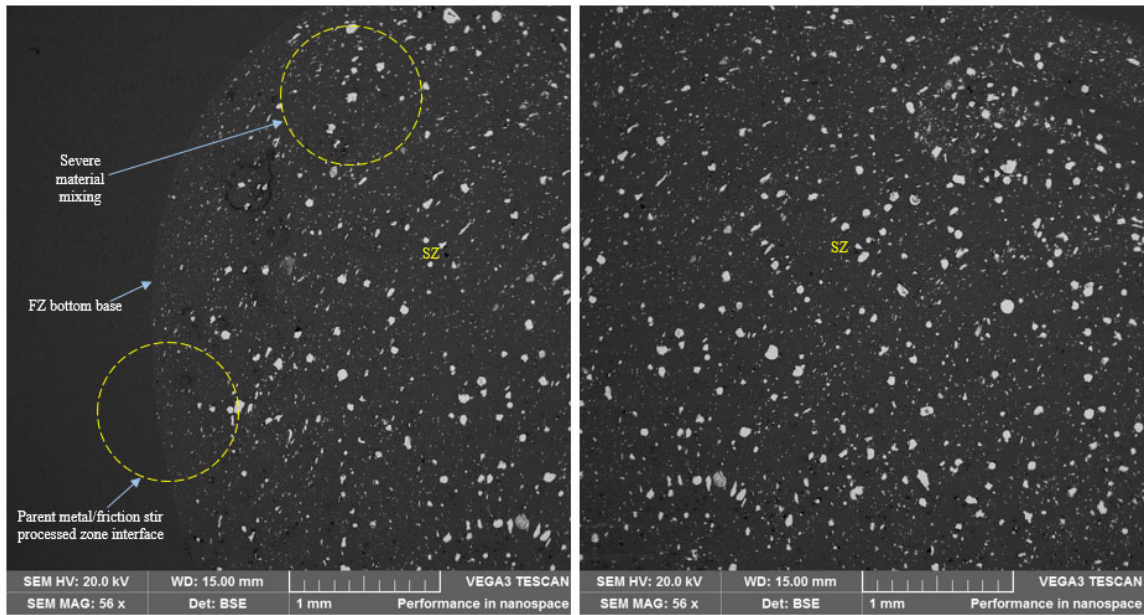
Fig. 3.5. SEM micrographs of the sample processed at 2100 rpm, 20 mm/min, 2.5º and 0.2 mm plunge depth
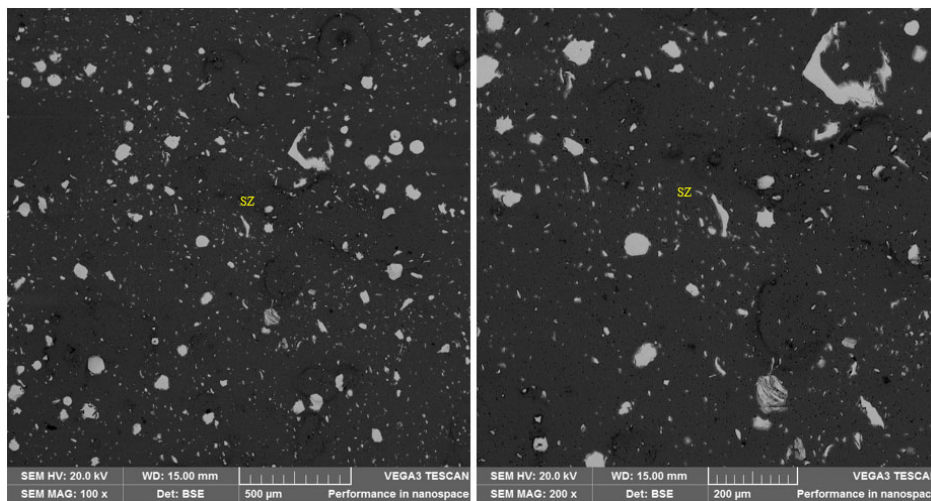

Fig. 3.6 SEM micrographs of the sample processed at 2100 rpm, 20 mm/min, 2.5º and 0.2 mm plunge depth – SZ

The 2450 rpm_20 mm/min processed micrographs – Fig. 3.7 and Fig. 3.8 show defect-free micrographs for samples processed at 2450 rpm. However, the increase in rotational speed was noted to initiate agglomeration of iron dominated 17-4 PH SS precipitates at the SZ-TMAZ interfaces. This could be as a result of the centrifugal effects, about the SZ center, that are associated with rotational speed processes. Very fine particles implanted in between and around the large iron dominated 17-4 PH SS precipitates were also noted. This showed the grain refinement capability of FSP. Smooth mechanical and metallurgical interfaces were also noticed on the micrographs. Mixed circular, elongated and irregular grains were also observed. These confirm the severe plastic deformation (SPD).

Fig. 3.7. SEM micrographs of the sample processed at 2450 rpm, 20 mm/min, 2.5º and 0.2 mm plunge depth – SZ
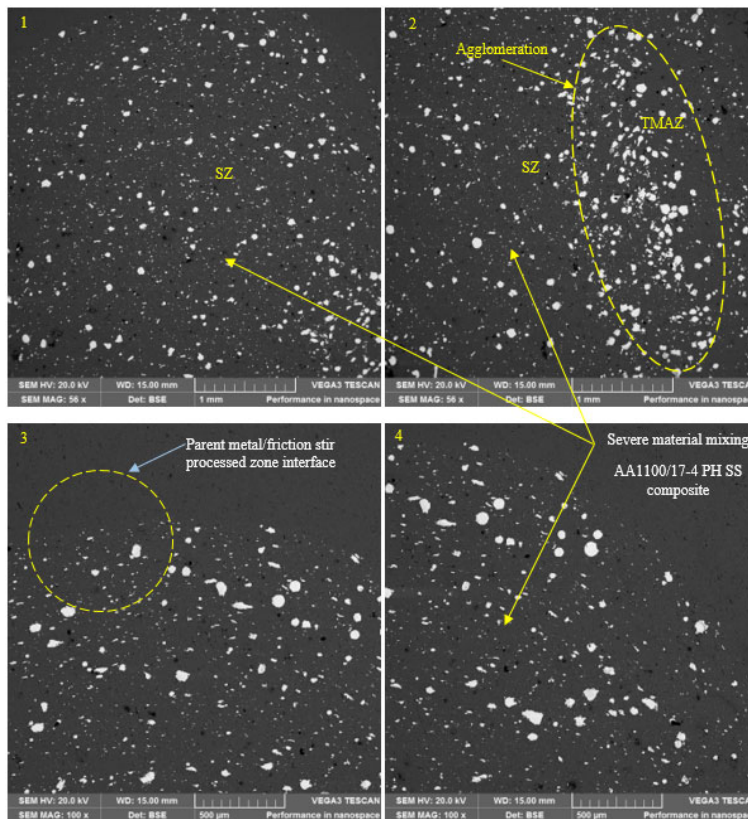
Fig. 3.8. SEM micrographs of the sample processed at 2450 rpm, 20 mm/min, 2.5º and 0.2 mm plunge depth – SZ

The 2800 rpm_20 mm/min processed micrographs: Fig. 3.9 and Fig. 3.10 show the defect-free SEM micrographs for samples processed at 2800 rpm. The micrographs were characterized by less packed agglomerated iron dominated 17-4 PH SS precipitates in the SZ-TMAZ interface. The micrographs had mixed elongated, circular, and irregular grains, which shows the potential of FSP to alter the

microstructure of the fabrications. Well mixed matrix and reinforcements confirm successful impregnation of reinforcements within the AA 1100 matrix.
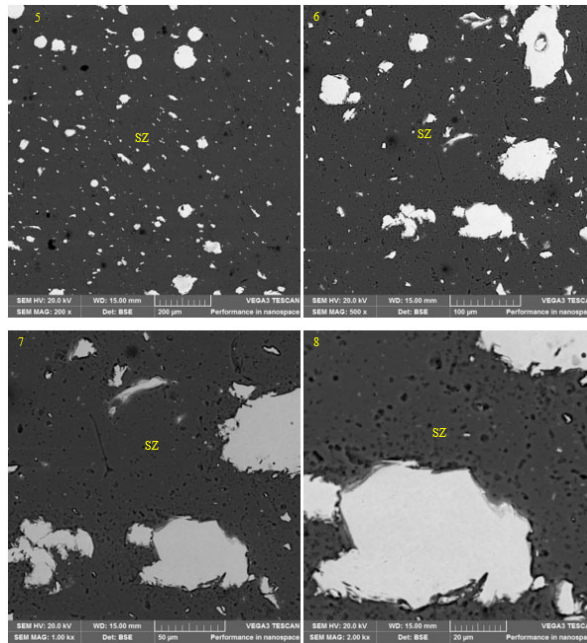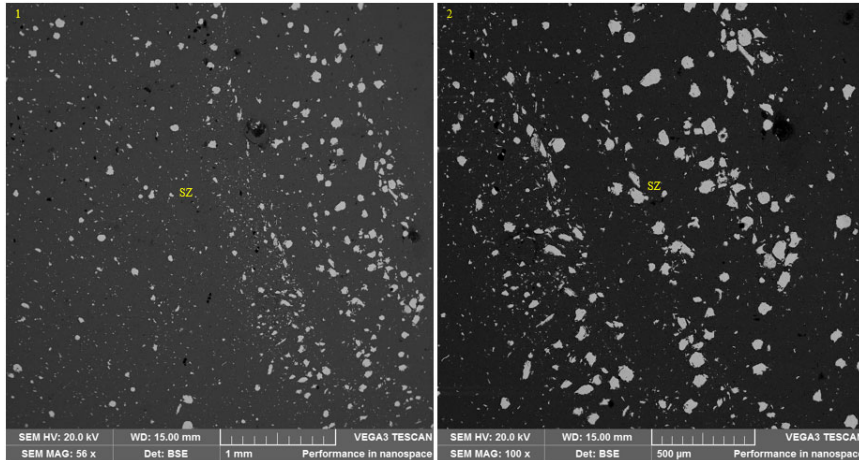

Fig. 3.9. SEM micrographs of the sample processed at 2800 rpm, 20 mm/min, 2.5º and 0.2 mm plunge depth
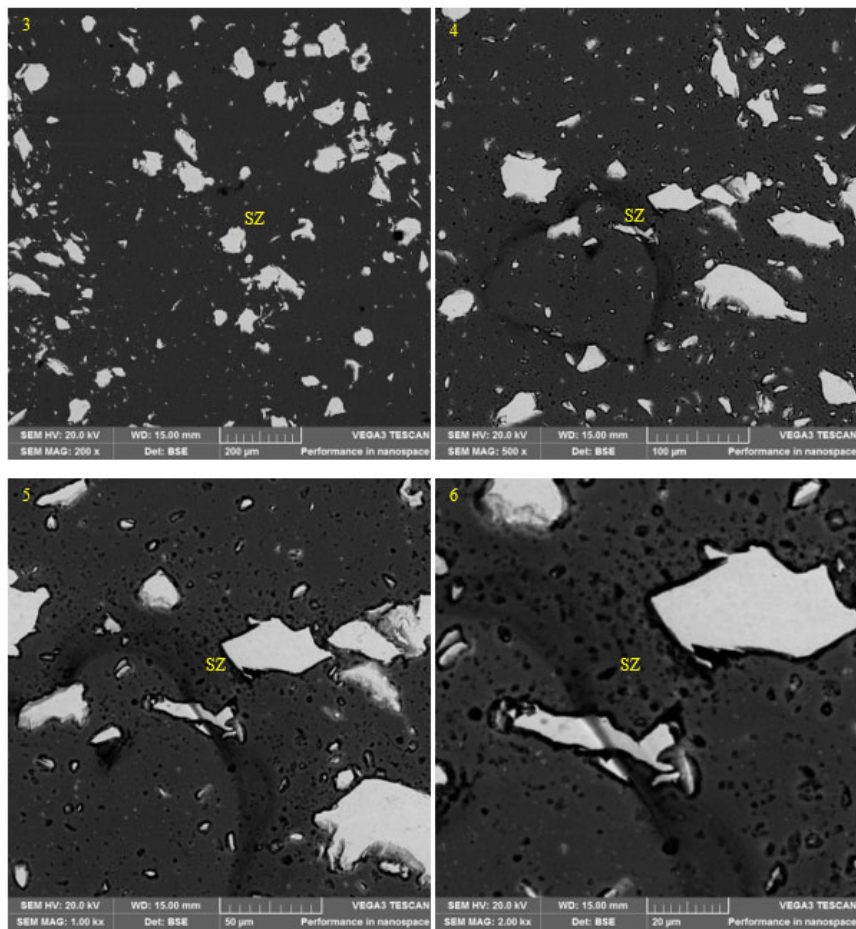
Fig. 3.10. SEM micrographs of the sample processed at 2800 rpm, 20 mm/min, 2.5º and 0.2 mm plunge depth

3.2 *Energy Dispersive Spectroscopy Studies*

Energy dispersive spectroscopy analysis was conducted to check the elemental composition of the friction stir processed composites, or in other words, to check for the impregnation of reinforcements into the AA1100 matrix. Fig. 3.11 shows the EDX results, which confirmed that the white contrast indeed

represented 17-4 PH SS elements. These were mainly dominated by iron, chromium, copper and nickel as shown by the white contrast spectra presented in parts (a) to (c) of the figure. As can be seen in the results obtained, the black contrast was dominated by Carbon. As was further noted in all the spectra presented in the figure, there were no spectra which had individual standalone elements, but a mixture. This was a confirmation of successful mixing of the 17-4 PH SS reinforcements and the aluminium matrix, which thus qualified FSP as an effective tool for fabrication of material composites. The agglomerated white contrasts were also analysed and were discovered to be the 17-4 PH SS reinforcements, as was observed on the distributed chemical elements. The employed process can therefore be recommended for development of AA1100/17-4 PH stainless steel composites.
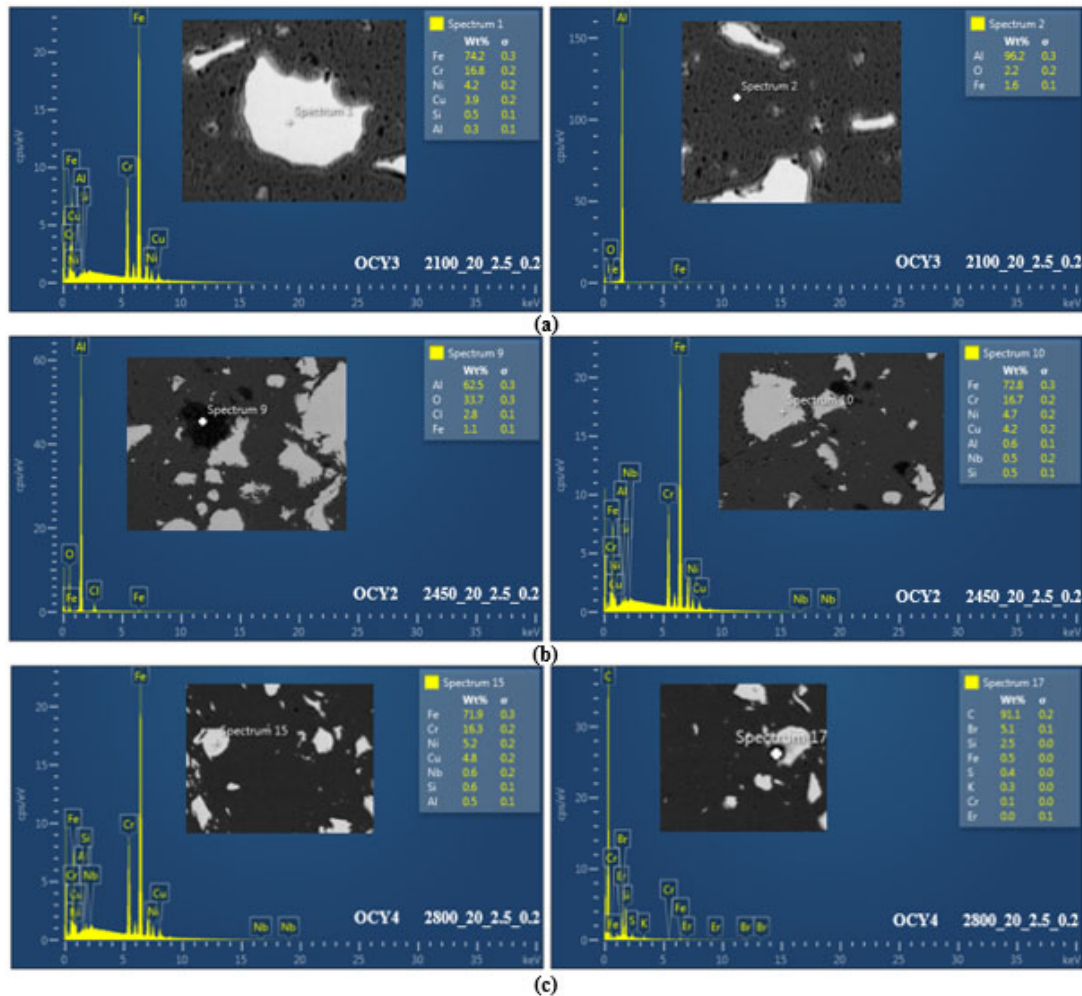
Fig. 3.11. Energy dispersive spectroscopy results

3.3 Tensile and Microhardness Behaviour

Tensile behaviour – Three base metal test pieces were tested and the results are shown in Fig. 3.12 (d) and Table 4. The BM UTS ranged from 91.74 MPa and 93.06 MPa, which yielded an average UTS of 92.23 MPa and an average percentage elongation of 38.5%, which are in agreement with the reported pure aluminium UTS values. The replicated tensile plots for the fabricated samples are shown in Fig. 3.12 (a) – (c), while the tensile test results are also summarized in Table 4. From the table, three specimens with FSP designation OCY3 had UTS values, UTS1, UTS2 and UTS3 of 85.51, 87.30 and 83.14 MPa respectively, which yielded an average UTS of 85.32 MPa, and a corresponding joint

efficiency of 92.51%, in comparison with the BM average UTS. The specimens had percentage elongations that ranged from 23 to 24.5%. OCY2 had UTS values, UTS1 of 89.97 and UTS2 of 89.48 MPa, and average UTS of 89.73 MPa, joint efficiency of 97.29 and an average percentage elongation of 32.4%. OCY4 had UTS values of UTS1 = 81.89, UTS2 = 83.11 and UTS3 = 83.60 MPa, an average UTS of 82.87 MPa, a joint efficiency of 89.85% and an average percentage elongation of 27.5%. The drop in percentage elongation can be attributed to the impregnation of the 17-4 PH stainless steel reinforcements, which are known to exhibit superior hardness properties, thus reducing the specimen ductility. As a result, the specimens fracture mode is likely to have transformed from a ductile-to-brittle mode. Although the attained UTS in the fabricated samples were slightly lower than that of the BM, their joint efficiencies are within acceptable limits.
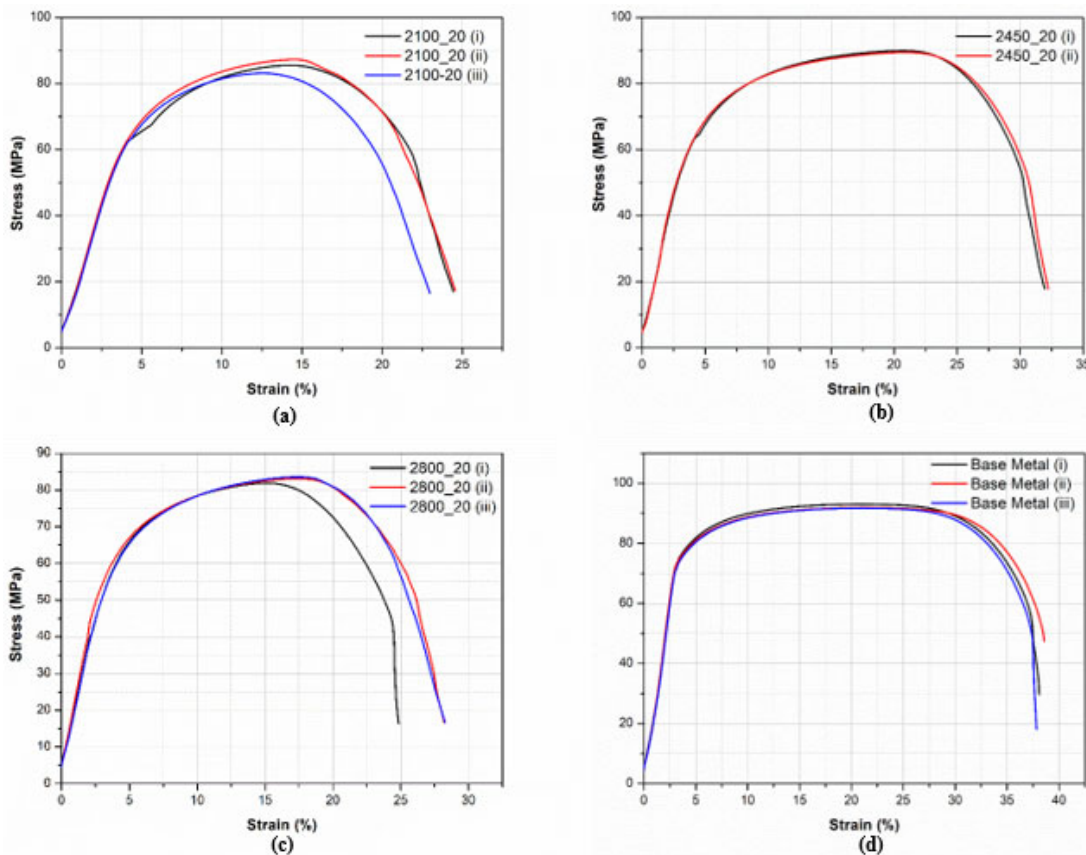
Fig. 3.12. Tensile test plots for the base metal and the fabricated samples

Table 4. Tensile results of friction stir processed tensile specimens

FSP Designation	Parameters rpm-mm/min-°-mm	Ultimate Tensile Strength (UTS) (MPa)			Average UTS (MPa)	Joint Efficiency (%)
		UTS1	UTS2	UTS3		
BM	--	93.06	91.88	91.74	92.23	100
OCY3	2100-20-2.5-0.2	85.51	87.30	83.14	85.32	92.51
OCY2	2450-20-2.5-0.2	89.97	89.48	--	89.73	97.29
OCY4	2800-20-2.5-0.2	81.89	83.11	83.60	82.87	89.85

Microhardness behaviour – Table 5 summarizes the obtained microhardness results, while Fig. 3.13 presents the obtained hardness plots for processed samples. Hardness was measured across the sectioned, ground and polished samples, from the AS to the RS. It was observed that the hardness gradually increased from the PM to the HAZ where sharp rises were noted in the TMAZ and in the SZ where it

was the highest. The highest hardness values of around 120, 104 and 90 HV 0.2 were recorded for the 2100, 2800 and 2450 rpm processes respectively. The obtained high hardness can also be as a result of indentations coinciding with the 17-4 PH SS precipitates. Uniform impregnation of the high-strength 17-4 PH SS reinforcements (as confirmed in microstructure evaluation studies) and severe plastic deformation (from the double pass process), which results in ultrafine grains in the SZ, also enhanced hardness. This gradually dropped in the TMAZ, the HAZ and PM where it was the lowest, which is in agreement with findings made by (Mahmoud & Tash, 2016; Abbasi & Bagheri, 2019; Wang, et al., 2020; Mazaheri, et al., 2020).

Table 5. HV 0.2 Microhardness data of the fabricated samples

| Distance from SZ Centre (mm) AS-RS	2100 rpm_20 mm/min	2450 rpm_20 mm/min	2800 rpm_20 mm/min
-13	30.4	41.2	34.0
-12	31.8	44.6	35.4
-11	34.4	52.4	34.8
-10	45.0	43.3	35.2
-9	49.3	49.2	32.5
-8	47.1	38.8	54.9
-7	66.8	41.6	54.8
-6	62.6	75.4	68.2
-5	30.0	51.8	60.2
-4	74.9	58.2	66.6
-3	69.1	74.3	51.5
-2	73.7	77.1	39.3
-1	91.0	78.1	56.2
0	69.2	85.0	34.3
1	119.5	70.5	35.3
2	76.3	79.3	62.8
3	66.2	54.0	104.2
4	74.2	68.5	71.3
5	65.8	63.8	77.4
6	70.5	39.6	36.2
7	54.0	44.1	32.5
8	33.1	41.4	38.3
9	34.1	61.1	31.3
10	38.3	67.3	32.8
11	33.8	37.2	32.5
12	32.7	57.8	34.8
13	33.5	62.5	34.1
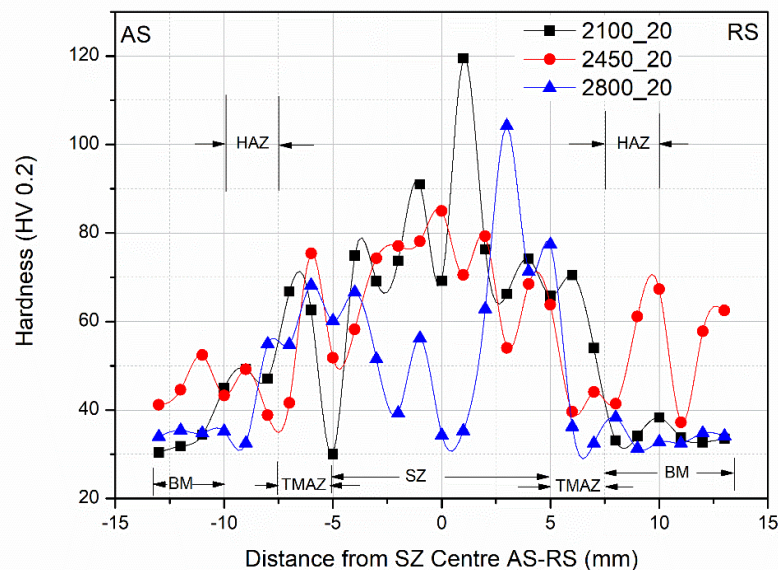
Fig. 3.13. Microhardness plots

The obtained hardness profiles were almost symmetrical about the SZs, towards both the AS and RS. The obtained hardness confirmed that friction stir processing successfully altered the microhardness of the parent metal, which is usually known to soften and weaken when worked, increasing it by around 4 times that of the PM (HV 28), in the SZ. As can be seen from the figure, all the obtained hardness profiles exhibited the shape of an inverted-V with a flat widened top, deviating from the W-shaped hardness profiles reported in literature (Manochehrian, et al., 2019).

3.4   Structural Analysis – XRD Results

Fig. 3. 14 to Fig. 3.16 show the obtained diffractograms. It was observed from the figures, that all the diffractograms were characterized by 5 pronounced peaks with different crystal planes. However, a common (111) crystal plane was observed in the diffractograms of all samples at around 39° 2θ range. All the diffractograms show mixed crystal planes on their second intense peak, a trend that was also seen in the third intense peak of the 2800 rpm diffractogram. This shows the existence of various phases in the peak, which is a further indication of successful impregnation of reinforcements within the matrix. As can be seen in the diffractograms, slight forward peak shifting with increase in rotational speed was also observed.
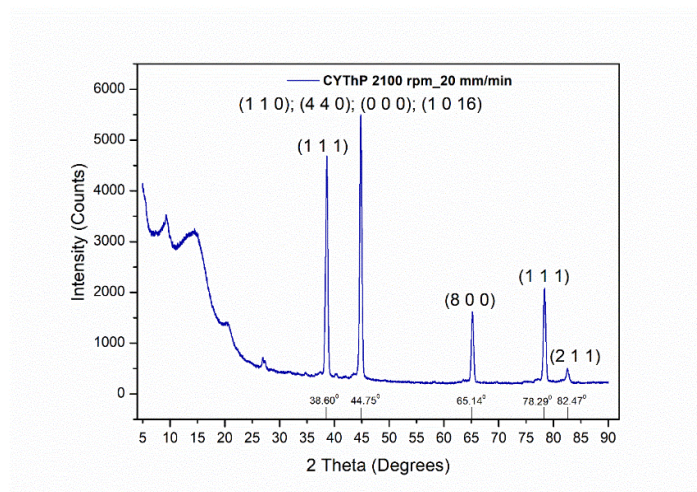

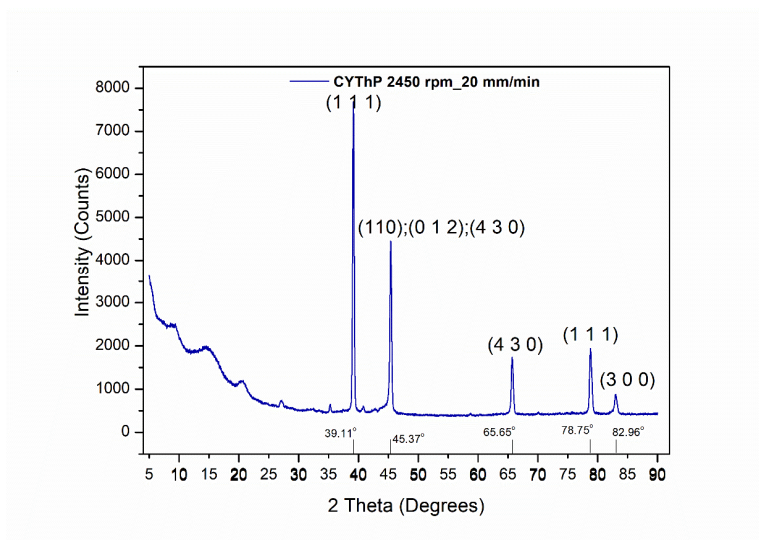**Fig. 3.14.** X-ray diffractogram for the 2100 rpm processed sample

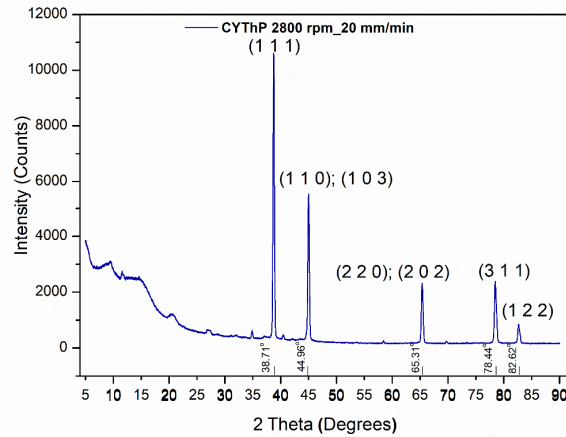**Fig. 3.15.** X-ray diffractogram for the 2450 rpm processed sample

Fig. 3.16. X-ray diffractogram for the 2800 rpm processed sample

Crystallinity studies were conducted and the results are presented in Table 6 and Table 7 for the 2100 rpm process, Table 9 and 10 for the 2450 rpm process, and Table 12 and 13 for the 2800 rpm process. The acquired crystallite size and micro strain were confirmed using the Scherrer equation and the Williamson-Hall equations presented in section 2.5, where the computation of dislocation density was also adopted (Ikumapayi, et al., 2020). Peaks in asterisks represent the major peaks while those without, represent minor peaks. As can be seen in the tables, the phases present confirm mixing of the continuous phase and the reinforcements. The attained crystallite sizes confirm the FSP grain refinement capability. The peak crystallite sizes ranged from 4.22 – 27.21 nm for the 2100 rpm process, 5.37 – 34.01 nm for the 2450 rpm process, and 4.40 – 41.34 nm for the 2800 rpm process. For the phase crystallite sizes, the 2100 rpm process recorded 17.98 – 19.97 nm, while the 2450 rpm process had 21.30 – 40.26 nm, and the 2800 rpm process yielded 22.21 – 40.47 nm. The quantitative studies on phase composition presented in Table 8, Table 11 and Table 14 for the 2100, 2450 and 2800 processes respectively all show well mixed Al matrix and 17-4 PH SS reinforcements. The high dislocation densities and micro strains obtained are an indication that the impregnated 17-4 PH stainless steel powder enhanced the AA1100 matrix (Ikumapayi, et al., 2020), as was also confirmed with the obtained tensile test and microhardness results.

Table 6. Peak properties of 2100 rpm processed sample

Peak Number	2-θ (°)	FWHM (°)	Size (nm)	Phase name
1	9.43	1.3831	6.02	Aluminium Copper (1,0,0)
2	14.69	1.9847	4.22	Aluminium Iron (1,1,-1), Aluminium Copper (1,1,0), Aluminium Copper Nickel (0,0,6)
3	20.50	1.5740	5.36	Aluminium Iron (1,1,2), Nickel Aluminium (2,1,1), Aluminium Tantalum Carbide (1,1,1), Aluminium Niobium Carbide (1,1,1), Aluminium Copper Nickel (0,0,9)
4	31.69	0.7250	11.90	Aluminium Iron Nickel (1,0,0), Aluminium Iron (5,1,-2), Nickel Aluminium (4,0,0), Aluminium Tantalum Carbide (2,1,1), Aluminium Niobium Carbide (2,1,1)
5*	38.60	0.4508	19.50	Aluminium, syn (1,1,1), Aluminium Iron (3,3,-2), Nickel Aluminium (4,2,2), Aluminium Tantalum Carbide (2,2,1), Aluminium Niobium Carbide (2,2,1), Aluminium Copper Nickel (1,0,13)
6*	44.75	0.4132	21.72	Aluminium, syn (2,0,0), Aluminium Iron Nickel (1,1,0), Aluminium Iron (4,2,-5), Nickel Aluminium (4,4,0), Chromium Iron (0,0,0), Aluminium Tantalum Carbide (2,2,2), Aluminium Niobium Carbide (2,2,2), Aluminium Copper Nickel (1,0,16)
7*	65.14	0.4091	24.07	Aluminium, syn (2,2,0), Aluminium Iron Nickel (2,0,0), Nickel Aluminium (8,0,0), Aluminium Tantalum Carbide (4,2,2), Aluminium Niobium Carbide (4,2,2), Aluminium Copper (6,1,1), Aluminium Copper Nickel (1,0,25)
8*	78.29	0.3861	27.71	Aluminium, syn (3,1,1), Nickel Aluminium (6,6,4), Aluminium Copper Nickel (1,2,14)
9*	82.47	0.4379	25.20	Aluminium, syn (2,2,2), Aluminium Iron Nickel (2,1,1), Nickel Aluminium (8,4,4), Aluminium Tantalum Carbide (4,4,2), Aluminium Niobium Carbide (4,4,2), Aluminium Copper Nickel (1,2,17)
10	87.19	2.0878	5.49	Nickel Aluminium (10,1,1), Aluminium Tantalum Carbide (6,1,1), Aluminium Niobium Carbide (6,1,1), Aluminium Copper (6,5,1), Aluminium Copper Nickel (1,1,30)

Table 7. Structural attributes of the phases obtained in the 2100 rpm processed sample

Phase name	Crystallite size (C) (nm)	Dislocation density (δ) (Lines/m^2) $\times 10^{15}$	Strain (ε) (%)
Aluminium, syn	17.98	3.0923	0.195
Aluminium Iron Nickel	19.95	2.5120	0.112
Aluminium Iron	19.75	2.5650	0.107
Nickel Aluminium	18.12	3.0470	0.191
Chromium Iron	19.27	2.6922	0.143
Aluminium Tantalum Carbide	18.12	3.0470	0.191
Aluminium Niobium Carbide	18.12	3.0470	0.191
Aluminium Copper	19.97	2.5073	0.112
Aluminium Copper Nickel	19.74	2.5666	0.108

Table 8. Quantitative analysis of phases present in the 2100 rpm processed sample

Phase name	Content(%)
Aluminum, syn	94.639794
Aluminum Iron Nickel	2.317694
Aluminum Iron	1.235683
Nickel Aluminum	0.360206
Chromium Iron	0.027957
Aluminum Tantalum Carbide	0.619981
Aluminum Niobium Carbide	0.478984
Aluminum Copper	0.215647
Aluminum Copper Nickel	0.104054

Table 9. Peak properties of 2450 rpm processed sample

Peak Number	2-θ (°)	FWHM (°)	Size (nm)	Phase name
1	9.51	1.5512	5.37	Tantalum Aluminium Carbide (0,0,2)
2	14.69	2.2250	3.76	Aluminium Niobium (1,1,0), sigma-Al Ta2 (1,1,0), Yarlongite (1,1,0)
3	20.54	1.4539	5.80	Copulate (0,1,0), Aluminium Niobium (1,0,1), sigma-Al Ta2 (1,0,1), Yarlongite (2,1,0)
4	32.01	1.0200	8.46	Cupalite (2,0,2), Aluminium Nickel (0,1,1), Aluminium Niobium (2,2,1), sigma-Al Ta2 (3,0,1), Yarlongite (3,2,0), Aluminium Chromium (1,1,0)
5*	39.11	0.2608	33.76	Aluminium, syn (1,1,1), Aluminium Niobium (3,3,0), Aluminium Chromium (1,1,1)
6	40.77	0.2701	32.77	Tantalum Aluminium Carbide (1,0,5), Aluminium Niobium (2,1,2), sigma-Al Ta2 (2,1,2), Yarlongite (1,0,2)
7*	45.37	0.2809	32.01	Aluminium, syn (2,0,0), Iron (1,1,0), Cupalite (3,1,0), Aluminium Nickel (0,1,2), sigma-Al Ta2 (4,3,0), Yarlongite (4,3,0), Aluminium Chromium (2,0,0)
8*	65.65	0.2970	33.24	Aluminium, syn (2,2,0), Iron (2,0,0), Aluminium Nickel (2,0,2), sigma-Al Ta2 (5,3,2), Yarlongite (6,1,2), Aluminium Chromium (2,2,0)
9*	78.75	0.3155	34.01	Aluminium Nickel (0,0,4), Tantalum Aluminium Carbide (1,1,10), Aluminium Niobium (6,5,1), sigma-Al Ta2 (6,4,2)
10*	82.96	0.3581	30.93	Aluminium Nickel (3,0,0), sigma-Al Ta2 (7,5,0), Yarlongite (6,6,0)

Table 10. Structural properties of the phases obtained in the 2450 rpm processed sample

Phase name	Crystallite size (C) (nm)	Dislocation density (δ) (Lines/m^2) $\times 10^{15}$	Strain (ε) (%)
Aluminium, syn	40.26	0.6170	0.168
Iron	25.02	1,5974	0.110
Cupalite	22.43	1,9877	0.075
Aluminium Nickel	27.28	1,3437	0.030
Tantalum Aluminium	24.57	1,6565	0.036
Aluminium Niobium	28.03	1,2728	0.106
sigma-Al Ta2	30.78	1,0555	0.075
Yarlongite	21.30	2,2042	0.110
Aluminium Chromium	40.24	0.6176	0.148

Table 11. Quantitative analysis of phases present in the 2450 rpm processed sample

Phase name	Content(%)
Aluminum, syn	82.458317
Iron	4.536884
Cupalite	0.000493
Aluminum Nickel	1.742856
Tantalum Aluminum Carbide	0.289244
Aluminum Niobium	0.182908
sigma-Al Ta2	0.301470
Yarlongite	8.922954
Aluminum Chromium	1.564874

Table 12. Peak properties of 2800 rpm processed sample

Peak No.	2-θ (°)	FWHM (°)	Size (nm)	Phase name
1	9.5633	1.5632	5.33	alpha-Al78 Cu48 Fe14 (1,1,0)
2	14.8753	1.9006	4.40	Aluminium Copper Nickel (0,0,6), Tantalum Aluminium Carbide (0,0,4), alpha-Al78 Cu48 Fe14 (2,0,0)
3	20.5516	1.1775	7.16	Aluminium Copper Nickel (0,0,9), alpha-Al78 Cu48 Fe14 (2,2,0)
4	28.6597	1.0724	7.99	Aluminium Copper Nickel (0,1,5), Tantalum Aluminium Carbide (0,0,8), alpha-Al78 Cu48 Fe14 (4,0,0)
5	32.0876	0.9128	9.46	Aluminium Copper Nickel (0,1,8), Tantalum Aluminium Carbide (1,0,0), Aluminium Nickel (0,1,1), alpha-Al78 Cu48 Fe14 (3,3,0)
6	34.8693	0.2109	41.23	Niobium Tantalum Carbide (1,1,1), Tantalum Aluminium Carbide (1,0,3), alpha-Al78 Cu48 Fe14 (3,3,2)
7*	38.71	0.2444	35.98	Aluminium, syn (1,1,1), alpha-Al78 Cu48 Fe14 (5,1,1), Aluminium Chromium (1,1,1)
8*	44.96	0.2510	35.78	Aluminium, syn (2,0,0), Tantalum Aluminium Carbide (0,0,12), Aluminium Nickel (1,1,0), Nickel Tantalum (1,0,3), alpha-Al78 Cu48 Fe14 (6,0,0), Aluminium Chromium (2,0,0)
9	58.3489	0.2348	40.47	Niobium Tantalum Carbide (2,2,0), Nickel Tantalum (2,0,0)
10*	65.31	0.2664	36.99	Aluminium, syn (2,2,0), Aluminium Copper Nickel (1,0,25), Aluminium Nickel (2,0,2), alpha-Al78 Cu48 Fe14 (8,2,2), Aluminium Chromium (2,2,0)
11*	78.44	0.2889	37.07	Aluminium, syn (3,1,1), Aluminium Copper Nickel (2,0,23), alpha-Al78 Cu48 Fe14 (8,5,3), Aluminium Chromium (3,1,1)
12*	82.62	0.2792	39.56	Aluminium, syn (2,2,2), Aluminium Copper Nickel (3,0,0), Aluminium Nickel (1,2,2), alpha-Al78 Cu48 Fe14 (7,7,3), Aluminium Chromium (2,2,2)

Table 13. Structural properties of the phases obtained in the 2800 rpm processed sample

Phase name	Crystallite size (C) (nm)	Dislocation density (δ) (Lines/m^2) $\times 10^{15}$	Strain (ε) (%)
Aluminium, syn	37.77	0.7010	0.092
Niobium Tantalum Carbide	40.47	0.6106	0.068
Aluminium Copper Nickel	22.21	2.0272	0.172
Tantalum Aluminium Carbide	33.13	9.1108	0.062
Aluminium Nickel	31.60	1.0014	0.068
Nickel Tantalum	30.66	1.0638	0.090
alpha-Al78 Cu48 Fe14	33.09	0.9133	0.022
Aluminium Chromium	37.77	0.7010	0.092

Table 14. Quantitative analysis of phases present in the 2800 rpm processed sample

Phase name	Content(%)	Phase name	Content(%)
Aluminum, syn	85.242117	Aluminum Nickel	1.719805
Niobium Tantalum Carbide	0.052062	Nickel Tantalum	0.082403
Aluminum Copper Nickel	10.770817	alpha-Al78 Cu48 Fe14	0.516448
Tantalum Aluminum Carbide	1.576646	Aluminum Chromium	0.039701

4. Conclusion

In this study, 17-4 PH stainless steel powder was used to reinforce the AA1100 matrix using 100% double pass FSP. The fabricated samples and specimens were examined for microstructure, elemental

composition, tensile testing and microhardness as well structural analysis using X-ray diffraction. Based on the attained results, the following conclusions can be drawn:

1) The employed double pass friction stir process produced defect-free micrographs
2) 17-4 PH stainless steel reinforcements were homogeneously distributed in the SZ at 2100 rpm
3) High rotational speeds of 2450 and 2800 rpm were both susceptible to particle agglomeration
4) The commonly known softening challenge of pure aluminium when worked was eliminated by the impregnated high-strength 17-4 PH stainless steel reinforcements in the SZ
5) The 17-4 PH stainless steel reinforcements enhanced the tensile and microhardness properties of the composites made
6) Increase in hardness reduced percentage elongation
7) The elemental composition obtained using EDS confirmed matrix and reinforcements mixing
8) Friction stir processing has the capability to refine grains to ultrafine size as was observed in the attained crystallite sizes
9) The obtained high dislocation densities and micro strains indicate high strength of the fabricated composites
10) While there were no much variations in the attained results, as the rotational speed was changed, all the three chosen rotational speeds produced highly acceptable results. Hence, the processing parameters employed in this work can be recommended.

References

Abbasi, M., Givi, M., & Bagheri, B. (2019). Application of vibration to enhance efficiency of friction stir processing. *Transactions of Nonferrous Metals Society of China*, *29*(7), 1393-1400.

Adamowski, J. & Szkodo, M., (2007). Friction Stir Welds (FSW) of aluminium alloy AW6082-T6. *Journal of Achievements in Materials and Manufacturing Engineering, 20*(1-2) 403-406.

Akinwamide, S. O., Akinribide, O. J. & Olubambi, P. A., (2021). Microstructural Evolution, Mechanical and Nanoindentation Studies of Stir Cast Binary and Ternary Aluminium Based Composites. *Journal of Alloys and Compounds, 850*, 1-13.

Alishavandia, M., Ebadi, M., Alishavandi, S. & Kokabi, A. H. (2020). Microstructural and Mechanical Characteristics of AA1050/Mischmetal Oxide In-situ Hybrid Surface Nanocomposite by Multi-pass Friction Stir Processing. *Surface & Coatings Technology, 388*.

Alishavandi, M., a, K. M. A. R., Alishavandi, M. E. S. & Kokabi, A. H. (2020). Corrosion-wear Behavior of AA1050/Mischmetal Oxides Surface Nanocomposite Fabricated by Friction Stir Processing. *Journal of Alloys and Compounds, 832*, 1-12.

Anand, R., & Sridhar, V. G. (2020). Studies on process parameters and tool geometry selecting aspects of friction stir welding–A review. *Materials Today: Proceedings*, *27*, 576-583.

ASTM-International (2015). Designation: B557M-15: Standard Test Methods for Tension Testing Wrought and Cast Aluminum- and Magnesium-Alloy Products (Metric), USA: ASTM International.

ASTM-International (2017). Designation: E92-17: Standard Test Methods for Vickers Hardness and Knoop Hardness of Metallic Materials, USA: ASTM International.

Bayode, A., Akinlabi, E. T., Pityana, S. & Shongwe, M. B. (2017). Effect of Scanning Speed on Laser Deposited 17-4PH Stainless Steel. Cape Town, South Africa, s.n.

Bourkhani, R. D., Eivania, A. R., Nateghi, H. R. & Jafariana, H. R. (2020). Effects of Pin Diameter and Number of Cycles on Microstructure and Tensile Properties of Friction Stir Fabricated AA1050-Al2O3 Nanocomposite. *Journal of Materials Research and Technology, 9*(3) 4506-4517.

Bourkhani, R. D., Eivani, A. R. & Nateghi, H. R. (2019). Through-thickness Inhomogeneity in Microstructure and Tensile Properties and Tribological Performance of Friction Stir Processed AA1050-Al2O3 Nanocomposite. *Composites Part B, 174*, 1-12.

Chelladurai, S. J. S., Kumar, S. S., Venugopal, N., Ray, A. P., Manjunath, T. C., & Gnanasekaran, S. (2021). A review on mechanical properties and wear behaviour of aluminium based metal matrix composites. *Materials Today: Proceedings*, *37*, 908-916.

Dutta, V., Thakur, L. & Singh, B. (2019). A Study on the Effect of Friction Stir Processing Technique for the Marine Applications. *Materials Today: Proceedings, 18,* 5048-5056.

Elfar, O. M. R., Rashad, R. M. & Megahed, H. (2016). Process Parameters Optimization for Friction Stir Welding of Pure Aluminium to Brass (CuZn30) using Taguchi Technique. *MATEC Web of Conferences, 43*, 1-6.

García-Vázquez, F., Vargas-Arista, B., Muñiz, R., Ortiz, J. C., García, H. H., & Acevedo, J. (2016). The role of friction stir processing (FSP) parameters on TiC reinforced surface Al7075-T651 aluminum alloy. *Soldagem & Inspeção*, *21*(4), 508-516.

Gunasekaran, T., Vijayan, S. N., Prakash, P., & Satishkumar, P. (2020). Mechanical properties and characterization of Al7075 aluminum alloy based ZrO2 particle reinforced metal-matrix composites. *Materials Today: Proceedings*.

Ikumapayi, O. M. & Akinlabi, E. T. (2019). Experimental Data on Surface Roughness and Force Feedback Analysis in Friction Stir Processed AA7075 e T651 Aluminium Metal Composites. *Data in brief, 23*, 1-14.

Ikumapayi, O. M., Akinlabi, E. T., Majumdar, J. D. & Akinlabi, S. A. (2020). Applications of Coconut shell Ash/Particles in Modern Manufacturing: A Case Study of Friction Stir Processing. In: K. Kumar & J. P. Davim, eds. Woodhead Publishing Reviews: Mechanical Engineering Series. s.l.:Woodhead Publishing 69-95.

Ikumapayi, O., Akinlabi, E., Sharma, A., Sharma, V., & Oladijo, O. (2020). Tribological, structural and mechanical characteristics of friction stir processed aluminium-based matrix composites reinforced with stainless steel micro-particles. *Engineering Solid Mechanics*, *8*(3), 253-270.

John, J., Shanmughanatan, S. P. & Kiran, M., 2016. Friction Stir Welding of Wrought Aluminium Alloys - A Short Review. *International Journal of Engineering Trends and Technology (IJETT), 32*(2) 76-81.

Ju, X., Zhang, F., Chen, Z., Ji, G., Wang, M., Wu, Y., ... & Wang, H. (2017). Microstructure of multi-pass friction-stir-processed Al-Zn-Mg-Cu alloys reinforced by nano-sized TiB2 particles and the effect of T6 heat treatment. *Metals*, *7*(12), 530.

Kiran, A. U. & Pravala, E. K. (2017). Experimental Investigations on Tribiological Properties of 6061-T6 Al Alloy by Via Friction Stir Processing. *International Journal of Advanced Engineering, Management and Science (IJAEMS), 3*(10) 995-1000.

ELSayed, E. M., Ahmed, M. M., Seleman, M. M. E., & EL-Nikhaily, A. E. (2017). Effect of Number of Friction Stir Processing Passes on Mechanical Properties of SiO2/5083Al Metal Matrix Nano-Composite. *Journal of Petroleum and Mining Engineering*, *19*(1), 10-17.

Kumar, A. S. & Praveen, V. (2017). A Review on Aluminium Based Metal Matrix Composites by Friction Stir Processing. *International Journal of Latest Engineering and Management Research (IJLEMR), 02*(07) 01-08.

Kumar, K., Gulati, P., Gupta, A. & Shukla, D. K. (2017). A Review of Friction Stir Processing of Aluminium Alloys Using Different Types of Reinforcements. *International Journal of Mechanical Engineering and Technology (IJMET), 8*(7) 1638-1651.

Kumar, S. N., Devarajaiah, R. M., & Prabhu, T. R. (2021). Review on aluminium based functionally graded composites. *Materials Today: Proceedings*, *39*, 1743-1749.

Liu, X. C., Zhen, Y. Q., Sun, Y. F., Shen, Z. K., Chen, H. Y., Wei, G. U. O., & Li, W. Y. (2020). Local inhomogeneity of mechanical properties in stir zone of friction stir welded AA1050 aluminum alloy. *Transactions of Nonferrous Metals Society of China*, *30*(9), 2369-2380.

Mahmoud, E. R. I. & Tash, M. M., 2016. Characterization of Aluminum-Based-Surface Matrix Composites with Iron and Iron Oxide Fabricated by Friction Stir Processing. *Materials, 9*(505) 1-13.

Manochehrian, A., Heidarpour, A., Mazaheri, Y. & Ghasemi, S. (2019). On the Surface Reinforcing of A356 Aluminum Alloy by Nanolayered Ti3AlC2 MAX Phase via Friction Stir Processing. *Surface & Coatings Technology, 377*(2019) 1-9.

Marazani, T., Akinlabi, E. T. & Madyira, D. M. (2020). Reduction of Excessive Flash in Friction Stir Processing of AA1100: An Experimental Observation Study. In: M. Awang, S. Emamian & F. Yusof, eds. *Advances in Material Sciences and Engineering. Lecture Notes in Mechanical Engineering*. Singapore: Springer 299-308.

Mazaheri, Y., Jalilvanda, M. M., Heidarpour, A. & Jahani, A. R. (2020). Tribological Behavior of AZ31/ZrO2 Surface Nanocomposites Developed by Friction Stir Processing. *Tribology International, 143*(2020) 1-14.

Mehta, M. G. & Vadher, J. A. (2020). Mechanical Characterization of Aluminum LM25 Based Metal Matrix Composite Made with Conventional Process. Materials Today: Proceedings 1-6.

El Mehtedi, M., Forcellese, A., Mancia, T., Simoncini, M., & Spigarelli, S. (2019). A new sustainable direct solid state recycling of AA1090 aluminum alloy chips by means of friction stir back extrusion process. *Procedia CIRP*, *79*, 638-643.

Mhaske, M. S. & Shirsat, U. M. (2020). An Investigation of Mechanical Properties of Aluminium Based Silicon Carbide (AlSiC) Metal Matrix Composite by Different Manufacturing methods. *Materials Today: Proceedings,* 1-7.

Miranda, R., Gandra, J., & Vilaça, P. (2013). Surface modification by friction based processes. *Morden Surface Engineering Treatments, Lisbon, INTECH*, 1-20.

Mouli, D. S. C., Rao, R. U. M. & Kumar, A. S. (2017). A Review on Aluminium Based Metal Matrix Composites by Friction Stir Processing. *International Journal of Engineering and Manufacturing Science, 7*(2) 203-224 .

Narayana, K. S. L., Benal, M. M. & Shivanand, H. K. (2020). Effect of Graphite on Aluminium Matrix Composites fabricated by Stir Casting Route – A Review. *Materials Today: Proceeding*s, 1-5.

Padhy, G. K., Wu, C. S. & Gao, S. (2018). Friction Stir Based Welding and Processing Technologies - Processes, Parameters, Microstructures and Applications: A Review. *Journal of Materials Science & Technology, 34,* 1-38.

Pai, K. R., Hebbale, A. M., Vishwanatha, J. S. & Sachin, B. (2020). Study of Tribological Properties on Aluminium Based Hybrid Composite Developed Through Microwave Energy. *Materials Today: Proceedings,* 1-6.

Rahmati, Z., Aval, H. J., Nourouzi, S. & Jamaati, R. (2020). Microstructural, Tribological, and Texture Analysis of Friction Surfaced Al-Mg-Cu clad on AA1050 Alloy. *Surface & Coatings Technology, 397,* 1-16.

Rao, D. S., Gupta, B. N. V. S. K. G., Rao, T. V. & Manikanta, J. E. (2020). Mechanical and Microstructural Behaviour of Aluminium/TiB2 Composites Fabricated Through Multi-pass Friction Stir Processing. *Materials Today: Proceedings,* 1-6.

Reddy, K. V., Naik, R. B., Reddy, G. M. & Kumar, R. A. (2020). Damping Capacity of Friction Stir Processed Commercial Pure Aluminium Metal. *Materials Today: Proceedings, 27*, 2061-2065.

Sampath, P., Parangodath, V. K., Udupa, K. R. & Kuruveri, U. B. (2015). Fabrication of Friction Stir Processed Al-Ni Particulate Composite and Its Impression Creep Behaviour. *Journal of Composites, Volume 2015* 1-9.

Shuvho, M. B. A., Chowdhury, M. A., Kchaou, M., Roy, B. K., Rahman, A., & Islam, M. A. (2020). Surface characterization and mechanical behavior of aluminum based metal matrix composite reinforced with nano Al2O3, SiC, TiO2 particles. *Chemical Data Collections*, *28*, 100442.

Singh, N. & Belokar, R. M. (2020). Tribological Behavior of Aluminum and Magnesium-based Hybrid Metal Matrix Composites: A State-of-Art Review. *Materials Today: Proceedings,* 1-7.

Srivastava, A. K., Kumar, N. & Dixit, A. R. (2021). Friction Stir Additive Manufacturing – An Innovative Tool to Enhance Mechanical and Microstructural Properties. *Materials Science & Engineering B, 263,* 1-25.

Vijayasarathi, P. & Selvam, D. (2014). Investigation and Analysis of Metallurgical and Mechanical Properties of AA1100 using FSW. *Journal of Environment and Earth Science, 4*(15) 90-95.

Wang, J., Lu, X., Cheng, C., Li, B., & Ma, Z. (2020). Improve the quality of 1060Al/Q235 explosive composite plate by friction stir processing. *Journal of Materials Research and Technology*, *9*(1), 42-51.

Yunusov, F. A. et al. (2020). Aluminum-based Composite Reinforced with Fullerene Soot. *Materials Today: Proceedings, 30*, 640-644.

Zamani, N. A. B. N., Iqbal, A. K. M. A. & Nuruzzaman, D. M. (2020). Tribo-mechanical Characterisation of Self-lubricating Aluminium Based Hybrid Metal Matrix Composite Fabricated via Powder Metallurgy. *Materialia, 14,* 1-10.